

# High-Performance All-Solid-State Lithium–Sulfur Batteries Enabled by Amorphous Sulfur-Coated Reduced Graphene Oxide Cathodes

Xiayin Yao, Ning Huang, Fudong Han, Qiang Zhang, Hongli Wan, Jean Pierre Mwizerwa, Chunsheng Wang,\* and Xiaoxiong Xu\*

Safety and the polysulfide shuttle reaction are two major challenges for liquid electrolyte lithium–sulfur (Li–S) batteries. Although use of solid-state electrolytes can overcome these two challenges, it also brings new challenges by increasing the interface resistance and stress/strain. In this work, the interface resistance and stress/strain of sulfur cathodes are significantly reduced by conformal coating  $\approx 2$  nm sulfur (S) onto reduced graphene oxide (rGO). An Li–S full cell consisting of an rGO@S-Li<sub>10</sub>GeP<sub>2</sub>S<sub>12</sub>-acetylene black (AB) composite cathode is evaluated. At 60 °C, the all-solid-state Li–S cell demonstrates a similar electrochemical performance as in liquid organic electrolyte, with high rate capacities of 1525.6, 1384.5, 1336.3, 903.2, 502.6, and 204.7 mA h g<sup>-1</sup> at 0.05, 0.1, 0.5, 1.0, 2.0, and 5.0 C, respectively. It can maintain a high and reversible capacity of 830 mA h g<sup>-1</sup> at 1.0 C for 750 cycles. The uniform distribution of the rGO@S nanocomposite in the Li<sub>10</sub>GeP<sub>2</sub>S<sub>12</sub>-AB matrix generates uniform volume changes during lithiation/delithiation, significantly reducing the stress/strain, thus extending the cycle life. Minimization of the stress/strain of solid cells is the key for a long cycle life of all-solid-state Li–S batteries.

## 1. Introduction

Lithium–sulfur (Li–S) batteries are considered to be one of the most promising candidates for hybrid electric vehicles and electric vehicles, as well as smart grids, due to high energy density;<sup>[1,2]</sup> sulfur has a five times higher theoretical specific capacity (1675 mA h g<sup>-1</sup>) than that of commercially used transition metal oxides, and is cheap, environmentally friendly, and abundant in nature.<sup>[3]</sup> However, traditional liquid Li–S batteries

suffer from safety problems arising from lithium anode and fast capacity fading due to the insulating nature of sulfur, the dissolution-induced polysulfide shuttle reaction, and large volume changes.<sup>[4–6]</sup> To address these issues, carbonaceous material<sup>[7,8]</sup> and conducting polymers<sup>[9]</sup> have been used to trap the high-order polysulfides in the cathodes; protective layers and electrolyte additives are employed for protection of metallic-lithium anodes from reactions with polysulfide.<sup>[10,11]</sup> However, the shuttle reaction still exists, and the safety issue induced by lithium dendrite is still a great challenge.

All-solid-state Li–S batteries can completely inhibit the dissolution of polysulfide, eliminate the polysulfide shuttle, and avoid lithium dendrite formation.<sup>[12–19]</sup> However, the use of rigid solid electrolytes in all-solid-state Li–S batteries also increases the stress/strain and inter-

face resistance and reduce the reaction kinetics.<sup>[20–22]</sup> The key challenge is to minimize stress/strain and to construct a robust electronic and ionic pathway in the sulfur cathode, due to the electronic/ionic insulating nature of sulfur. For enhancing the electronic conductivity and reducing the electronic contact resistance, Kobayashi et al. synthesized a sulfur and acetylene black (AB) nanocomposite cathode using a gas-phase mixing method, and reported a reversible capacity of 900 mA h g<sup>-1</sup> at a current density of 0.013 mA cm<sup>-2</sup> in all-solid-state batteries.<sup>[23]</sup> The sulfur and carbon-nanofibers composite cathode also shows a high capacity in the all-solid-state Li–S batteries.<sup>[24]</sup> To ensure high ionic conduction in the sulfur cathode, Lin et al. synthesized core-shell structured lithium–sulfide nanoparticles with an Li<sub>3</sub>PS<sub>4</sub> electrolyte as shell, showing six orders of magnitude higher in ionic conductivity than that of bulk lithium–sulfide. Excellent cyclic performance was demonstrated for all-solid-state Li–S batteries at 60 °C.<sup>[13]</sup> By incorporation of five sulfur atoms in the Li<sub>3</sub>PS<sub>4</sub> electrolyte, the Li<sub>3</sub>PS<sub>4</sub>S<sub>5</sub> cathode with loading density of 0.25–0.6 mg cm<sup>-2</sup> exhibits excellent cycling stability for all-solid-state Li–S batteries.<sup>[14]</sup> These studies demonstrate that a close contact of the nanosulfur, either to carbon or to electrolytes, and uniformly distributing these composites into an ionic/electronic conducting matrix, can significantly improve the electrochemical performances of solid-state Li–S cell because the nano-sulfur contacts both the highly ionic and

Dr. X. Y. Yao, N. Huang, Q. Zhang, H. L. Wan, J. P. Mwizerwa, Prof. X. X. Xu

Ningbo Institute of Materials Technology and Engineering  
Chinese Academy of Sciences  
Ningbo 315201, P. R. China  
E-mail: xuxx@nimte.ac.cn

F. D. Han, Prof. C. S. Wang  
Department of Chemical and Biomolecular Engineering  
University of Maryland  
College Park 20142, MD, USA  
E-mail: cswang@umd.edu

N. Huang  
Nano Science and Technology Institute  
University of Science and Technology of China  
Suzhou 215123, P. R. China

DOI: 10.1002/aenm.201602923

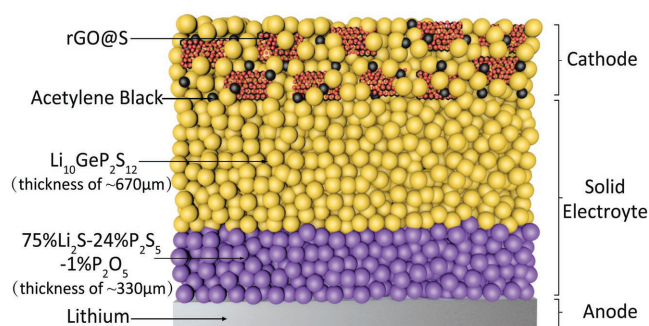


**Figure 1.** Schematic diagram of an all-solid-state lithium-sulfur battery.

electronic conducted matrix in the cathode. In addition, uniformly dispersing nano-sulfur/carbon in a mixed conductive cathode can also reduce and make the volume change of sulfur uniform during charge/discharge, which can reduce the stress/strain, thus largely enhancing cycle stability in all-solid-state Li-S batteries. However, the impact of the volume change of the sulfur cathode on cycle stability of solid-state Li-S batteries has not been reported.

In this work, we reported a unique sulfur cathode fabricated by deposition of nanoamorphous sulfur on reduced graphene oxide (rGO) to maintain high electronic conduction, and then uniformly distribute the rGO@S nanocomposite into mixed conducting  $\text{Li}_{10}\text{GeP}_2\text{S}_{12}$ -acetylene black composite to also achieve high ionic conductivity and low stress/strain. The reduced graphene oxide serves as electronic conduction network and could buffer the volume expansion and improve structure stability of sulfur; while the reduced particle size of sulfur could shorten the pathways for lithium-ion insertion/extraction, increase the contact area with electrolytes, reduce and uniform the stress/strain, evidenced by minimizing the pulverization/crack in both cathode and electrolyte layers. In addition,  $\text{Li}_{10}\text{GeP}_2\text{S}_{12}$  with high ionic conductivity of  $8.27 \times 10^{-3} \text{ S cm}^{-1}$  at room temperature is used as an electrolyte both in the cathode and electrolyte layer to enhance ionic conductivity in the cell. Since the  $\text{Li}_{10}\text{GeP}_2\text{S}_{12}$  electrolyte is not stable with the lithium anode, a lithium compatible 75% $\text{Li}_2\text{S}$ -24% $\text{P}_2\text{S}_5$ -1% $\text{P}_2\text{O}_5$  electrolyte layer was inserted between the  $\text{Li}_{10}\text{GeP}_2\text{S}_{12}$  electrolyte layer and lithium anode to avoid the reaction between lithium metal and  $\text{Li}_{10}\text{GeP}_2\text{S}_{12}$ ,<sup>[25]</sup> as shown in **Figure 1**. The resultant all-solid-state Li-S batteries show high capacity, good cycling stability, and excellent rate capability. The

strategy that coating a nanolayer of sulfur onto electronic conductive rGO and uniformly distributing them into highly conductive  $\text{Li}_{10}\text{GeP}_2\text{S}_{12}$  presented here provides an efficient way to obtain high-performance Li-S batteries with excellent safety.

## 2. Results and Discussion

**Figure 2a** and **Figure S1** (Supporting Information) show the X-ray diffraction (XRD) patterns of the rGO@S-40, rGO@S-50, rGO, and sublimed sulfur. No obvious diffraction peaks are detected in rGO@S-40 and rGO@S-50 samples (**Figure 2a**), indicating the amorphous structure of rGO@S composites. However, amorphous rGO@S-40 can change to crystalline rGO@S-40 when the reaction time is extended from 2 to 5 min (**Figure S1**, Supporting Information). In **Figure S1** (Supporting Information), the main diffraction peaks of crystal rGO@S-40 sample at  $2\theta = 15.39^\circ, 23.07^\circ, 25.83^\circ, 26.71^\circ$ , and  $31.39^\circ$  are indexed to the diffraction from the (113), (222), (026), (311), and (044) planes of crystal sulfur, respectively (JCPDS card no.78-1889).<sup>[26]</sup> Raman spectroscopy was also conducted to further characterize the structure of amorphous rGO@S-40, and compared it with rGO and crystal sublimed sulfur (**Figure 2b**). The sublimed sulfur displays sharp characteristic peaks at 154, 219, and  $473 \text{ cm}^{-1}$ , which reflect the bending and the stretching of S-S bonds, respectively.<sup>[27]</sup> Raman spectroscopy of rGO is characterized by the D band at around  $1350 \text{ cm}^{-1}$  and G band at about  $1580 \text{ cm}^{-1}$ , corresponding to disorders/defects and graphitic degree, respectively.<sup>[28]</sup> Both characteristic peaks for sulfur and rGO are observed in amorphous rGO@S-40, confirming the existence of both sulfur and rGO in the amorphous rGO@S-40 composite. Similar results are obtained for crystal rGO@S-40 and amorphous rGO@S-50 samples (**Figure S2**, Supporting Information). In addition, the intensity ratio of D/G band varies with the structure of the carbon.<sup>[29]</sup> The higher the D/G band intensity ratio, the poorer the electronic conductivity. The intensity ratios of D/G band are 1.53 for the amorphous rGO@S-40 composites and 1.04 for rGO, indicating that electronic conductivity of the amorphous rGO@S-40 significantly reduced compared with that of rGO due to the insulation of sulfur in the composite. Moreover, with increasing sulfur content from 40 to 50 wt%, the intensity ratio of D/G band further increased from 1.53 in amorphous rGO@S-50 to 1.59 in amorphous rGO@S-50 composite, which indicates that the electronic conductivity is further reduced.

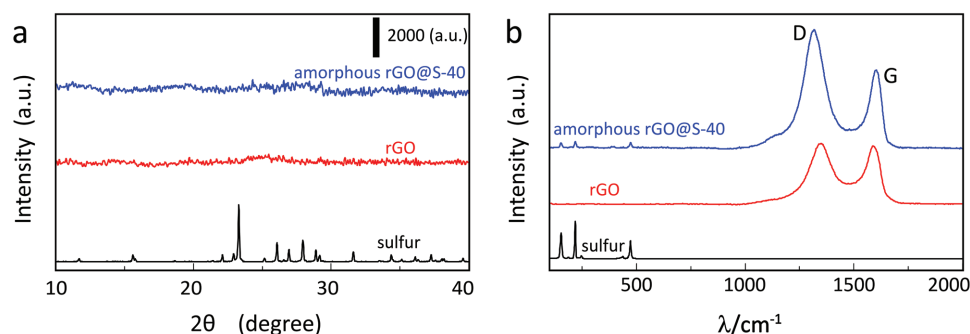


**Figure 2.** a) XRD patterns and b) Raman spectra of the amorphous rGO@S-40, rGO, and sublimed sulfur.

The morphology of amorphous rGO@S composite was characterized using scanning electron microscope (SEM). As shown in **Figure 3**, the thin rGO in amorphous rGO@S composite has a nanosheet structure with a lateral size of several micrometers and is translucent under electron beam (Figure 3a). However, no sulfur particles could be observed on the nanosheets both in SEM and transmission electron microscopy (TEM) images (Figure S3, Supporting Information), while energy dispersive X-ray (EDX) results in Figure 3b,c confirm the existence of both carbon and sulfur in amorphous rGO@S-40 composite, and both elements homogeneously distributed throughout the rGO nanosheet. The absence of sulfur in SEM and TEM images is attributed to the sublimation of sulfur from rGO under the high vacuum conditions and beam damage of SEM and TEM experiments.<sup>[30]</sup> Atomic force microscopy (AFM) without vacuum was further conducted to confirm the existence of sulfur and determine the thickness of sulfur layer. **Figure 4a** clearly shows the nanosheet structure of amorphous rGO@S-40 composite, which is consistent with SEM and TEM results. Magnified AFM image in **Figure 4b** clearly shows the existence of sulfur particles on rGO. Considering sulfur particles uniformly deposited on both sides of rGO surface (Figure 4b), the thickness of the sulfur layer estimated from the height profiles is below 2 nm by subtracting the thickness of rGO (Figure 4c,d). Besides, the thickness of sulfur layer varies with the nature of sulfur. The thickness of sulfur increases to about 6 nm for

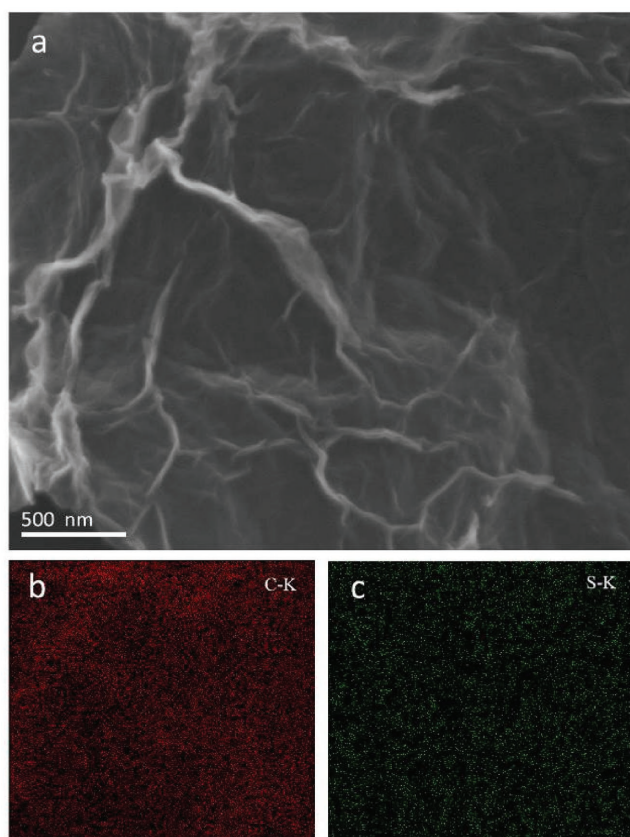


**Figure 3.** SEM image of a) the amorphous rGO@S-40 composite and corresponding EDX mapping for b) carbon and c) sulfur.

crystal rGO@S-40 composite, as shown in Figure S4 (Supporting Information).

The sulfur content in rGO@S composite was determined by thermogravimetric analysis (TGA) and was shown in Figure S5 (Supporting Information). The sublimed sulfur loses weight in the temperature range of 100–350 °C.<sup>[26,31]</sup> The sulfur contents in the amorphous rGO@S-40, crystal rGO@S-40, and amorphous rGO@S-50 samples are 43, 41, and 51 wt%, respectively. The high-frequency infrared ray carbon–sulfur analyzer also confirms the TGA results, showing 41, 42, and 51 wt% for amorphous rGO@S-40, crystal rGO@S-40, and amorphous rGO@S-50 samples, respectively.

The electrochemical performances of amorphous rGO@S-40 were investigated at 60 °C using all-solid-state lithium cells. **Figure 5a** shows cyclic voltammogram (CV) curves of amorphous rGO@S-40 composite at 60 °C in the potential range from 1.0 to 3.0 V at a scan rate of 0.1 mV s<sup>−1</sup>. In the first cathodic scan, one remarkable reduction peak at 1.95 V is detected due to the reduction of S<sub>8</sub> molecules to the Li<sub>2</sub>S. Meanwhile, an oxidation peak at ≈2.35 V is observed during the anodic process, corresponding to the oxidation of lithium sulfides back to sulfur. In the subsequent cycles, both reduction and oxidation peaks slightly shift to higher potential, while the peak currents and the enclosed areas in the following cycles are almost identical to each other after the second cycle, indicating the good electrochemical reversibility of the amorphous rGO@S-40 composite electrode. The absence of high voltage peaks demonstrated that the intermediate polysulfides are not formed in the charge/discharge of all-solid state Li–S cell. **Figure 5b** shows the galvanostatic discharge–charge profiles of the amorphous rGO@S-40 in all-solid-state Li–S battery under 0.05 C at 60 °C. Only one discharge plateau at around 2.1 V and one charge plateau at around 2.3 V are observed, which is different from that of traditional organic liquid electrolyte Li–S batteries. For a typical Li–S battery in an organic liquid electrolyte, the discharge curves generally show obvious two plateaus at about 2.4 and 2.1 V, indicating the two stages of the reduction of sulfur to Li<sub>2</sub>S<sub>n</sub> (4 < n ≤ 8) and Li<sub>2</sub>S<sub>2</sub> or Li<sub>2</sub>S. During the charging process, Li<sub>2</sub>S is delithiated to form Li<sub>2</sub>S<sub>4</sub> and eventually S<sub>8</sub>.<sup>[32,33]</sup> Clearly, the sulfur redox chemistry in all-solid-state Li–S batteries is quite different from that in liquid electrolyte Li–S cell. It has been reported that use of inorganic solid electrolytes to replace liquid electrolytes in the Li/S cell could suppress the formation of polysulfides.<sup>[13–15,23,24,34]</sup> Sharma investigated the equilibrium phase in the lithium–sulfur system and found that in addition to sulfur, only one solid compound of Li<sub>2</sub>S, rather than Li<sub>2</sub>S<sub>2</sub> or Li<sub>2</sub>S<sub>n</sub> (4 ≤ n ≤ 8), was observed in the range of composition investigated,<sup>[35]</sup> indicating only Li<sub>2</sub>S was formed during the solid-state reaction. The ex situ S K-edge X-ray absorption fine structure measurements reported by Takeuchi et al. for all-solid-state lithium secondary battery with Li<sub>2</sub>S–carbon composite positive electrode further confirms the direct electrochemical reaction Li<sub>2</sub>S ↔ 2Li + S.<sup>[34]</sup> The only one plateau (Figure 5b) related to the S<sub>8</sub> transformed into S<sup>2−</sup> in the all-solid-state Li–S battery strongly supports the direct reaction mechanism between sulfur and Li<sub>2</sub>S during the discharge/charge process in the solid-state Li–S cell, which is in accordance with the CV scan in Figure 5a. The amorphous rGO@S-40 composite shows an initial discharge capacity as high as 2049 mA h g<sup>−1</sup>, which



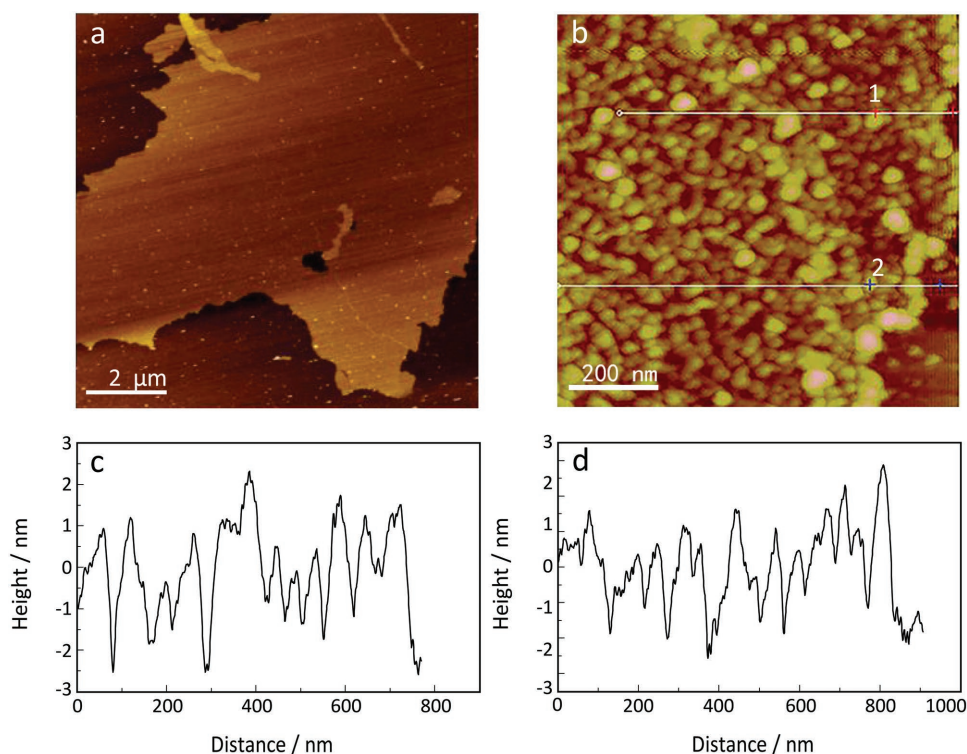


**Figure 4.** AFM images of a,b) amorphous rGO@S-40 composite on a Si substrate and corresponding height profiles at lines c) 1 and d) 2 in (b).

is much higher than the theoretical specific capacity of sulfur, and could be attributed to the capacity contribution from the  $\text{Li}_{10}\text{GeP}_2\text{S}_{12}$  electrolyte.<sup>[36]</sup> As shown in Figure S6a (Supporting Information), the initial discharge capacity of  $\text{Li}_{10}\text{GeP}_2\text{S}_{12}$  electrolyte with the same amount of carbon black as in rGO@S-40

cathode but without the active material of rGO@S-40 is  $420 \text{ mA h g}^{-1}$ , while the reversible specific capacity is only around  $10 \text{ mA h g}^{-1}$  in the following charge/discharge cycles. The low reversible capacity of  $\text{Li}_{10}\text{GeP}_2\text{S}_{12}$  is due to the narrow cut-off voltage window of 1.5–2.8 V. When the  $\text{Li}_{10}\text{GeP}_2\text{S}_{12}$

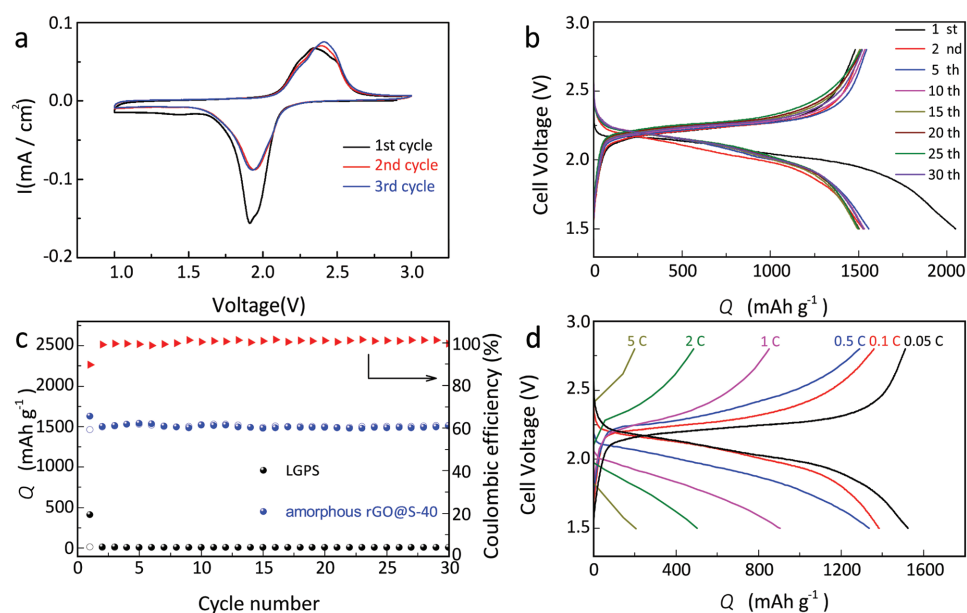


**Figure 5.** a) Cyclic voltammogram of the amorphous rGO@S-40 composite in all-solid-state cell at  $60^\circ\text{C}$ . b) Galvanostatic discharge/charge profiles of the amorphous rGO@S-40 composite in all-solid-state Li–S battery under 0.05 C at  $60^\circ\text{C}$ . c) Cycling performances of the amorphous rGO@S-40 composite by subtracting the  $\text{Li}_{10}\text{GeP}_2\text{S}_{12}$  contribution. d) Galvanostatic discharge/charge profiles for the amorphous rGO@S-40 composite in all-solid-state Li–S battery under different C rates at  $60^\circ\text{C}$ .

electrolyte is cycled between 1.0 and 3.5 V, over 400 mA h g<sup>-1</sup> of capacity can be obtained after 15 cycles (Figure S6b, Supporting Information). By subtracting the capacity contribution from Li<sub>10</sub>GeP<sub>2</sub>S<sub>12</sub> obtained in the potential range of 1.5–2.8 V, the initial discharge capacity of the amorphous rGO@S-40 composite is 1629 mA h g<sup>-1</sup>, corresponding to a sulfur utilization of 97.3%. Meanwhile, the amorphous rGO@S-40 composite shows an initial charge capacity of 1465 mA h g<sup>-1</sup> with a high Coulombic efficiency of 90%. During the following cycles, the discharge/charge capacities stabilize at ≈1500 mA h g<sup>-1</sup> and the Coulombic efficiency is increased to almost 100%, as shown in Figure 5c. The excellent capacity retention of the amorphous rGO@S-40 composite electrode could benefit from the avoidance of intermediate polysulfide shuttle and less stress/strain due to uniform volume change in the all-solid-state cell. The amorphous rGO@S-40 composites also show exceptional rate capability. Figure 5d displays charge/discharge profile of amorphous rGO@S-40 at different currents from 0.05 to 5 C after two activation cycles. The amorphous rGO@S-40 composites can provide 1525.6, 1384.5, 1336.3, 903.2, 502.6, and 204.7 mA g<sup>-1</sup> at 0.05, 0.1, 0.5, 1.0, 2.0, and 5.0 C, respectively. The rate performance of amorphous rGO@S-40 in all-solid-state Li–S batteries is comparable to that of Li–S cell in organic liquid electrolytes.<sup>[33,37,38]</sup>

The impact of sulfur structure, sulfur loading, and operation temperature on the cycling stability rGO@S cathodes was also investigated. **Figure 6a** compares the cycling stability of the amorphous rGO@S-40, amorphous rGO@S-50, and crystal rGO@S-40 composites at 60 °C and 0.5 C rate. All three cathodes show stable capacity for 30 cycles, but the amorphous rGO@S-40 shows the highest capacity of 1340 mA h g<sup>-1</sup>. Crystal rGO@S-40 shows a lower capacity (987 mA h g<sup>-1</sup>) than amorphous rGO@S-40 (1340 mA h g<sup>-1</sup>) due to increased sulfur thickness from 2 nm for amorphous rGO@S-40 (Figure 4b) to 6 nm for crystal rGO@S-40 (Figure S4, Supporting Information).

Increase of sulfur loading from 40 to 50 wt% significantly reduces the capacity from 1340 to 779 mA h g<sup>-1</sup> due to reduced electronic and ionic conductivity of sulfur (Figure 6a). Since amorphous rGO@S-40 shows the best performance in amorphous rGO@S-50 and crystal rGO@S-40, amorphous rGO@S-40 cathode was selected to study the impact of temperature on the cycle stability at a high current density of 1.0 C. Figure 6b shows the cycling stability of the amorphous rGO@S-40 composites at 25, 60, and 100 °C. The detail charge/discharge curves of amorphous rGO@S-40 in temperature of 25, 60, and 100 °C were shown in Figure 6c–e. Amorphous rGO@S-40 shows much higher capacity at 60 °C than that at 25 and 100 °C. At 60 °C, the capacity slightly increases from 930 to 1077 mA h g<sup>-1</sup> in the first 100 cycles (Figure 6b) due to an activation process,<sup>[15,39]</sup> which has been reported in the Li–S batteries.<sup>[40,41]</sup> The capacity begins to slowly decline after 400 cycles but still maintains 830 mA h g<sup>-1</sup> at 750 cycles. The capacity decay rate of 0.015% per cycle is lower than liquid electrolyte Li–S cells.<sup>[42,43]</sup> Furthermore, the Coulombic efficiency is close to 100% after the first 20 cycles, indicating the high reversibility. However, at both 25 and 100 °C, amorphous rGO@S-40 composites show a low discharge capacity (Figure 6c,e), and quick capacity decay to 100 mA h g<sup>-1</sup> after 60 cycles. In addition, the charge/discharge curves of amorphous rGO@S-40 at both 25 and 100 °C show a higher overpotential than that at 60 °C.

To understand the mechanism for poor performance of amorphous rGO@S-40 composite at 25 and 100 °C, impedance change of Li<sub>10</sub>GeP<sub>2</sub>S<sub>12</sub>/75%Li<sub>2</sub>S-24%P<sub>2</sub>S<sub>5</sub>-1%P<sub>2</sub>O<sub>5</sub> bilayer electrolyte (Figure S7a, Supporting Information) and the impedance evolution of Li–S cell using amorphous rGO@S-40 cathode (**Figure 7a** and Figure S7b, Supporting Information) at different temperatures from 25 to 100 °C were separately measured. The electrochemical impedance spectroscopy (EIS) of Li–S cell was measured after one activation cycle between 1.5 and 2.8 V at 0.05 C and 25 °C (Figure S7c, Supporting

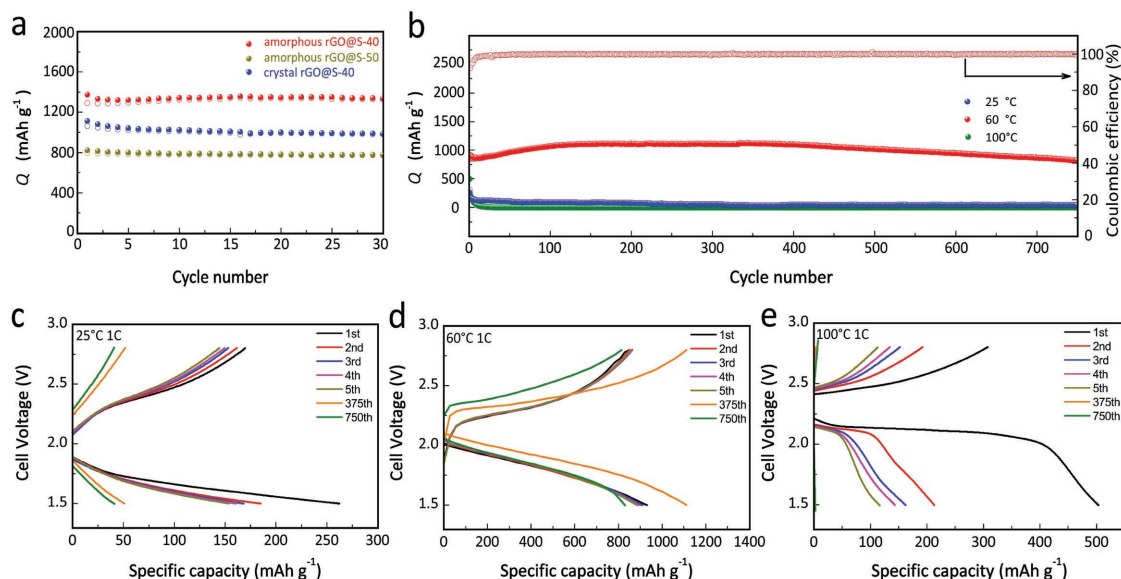


**Figure 6.** a) Cycling performances of amorphous rGO@S-40, amorphous rGO@S-50, and crystal rGO@S-40 under 0.5 C at 60 °C. b) Cycling performances of amorphous rGO@S-40 composites under the high rate of 1.0 C and corresponding Coulombic efficiencies at 60 °C. Galvanostatic discharge/charge profiles for the amorphous rGO@S-40 composite in all-solid-state Li–S battery under 1.0 C at c) 25, d) 60, and e) 100 °C.

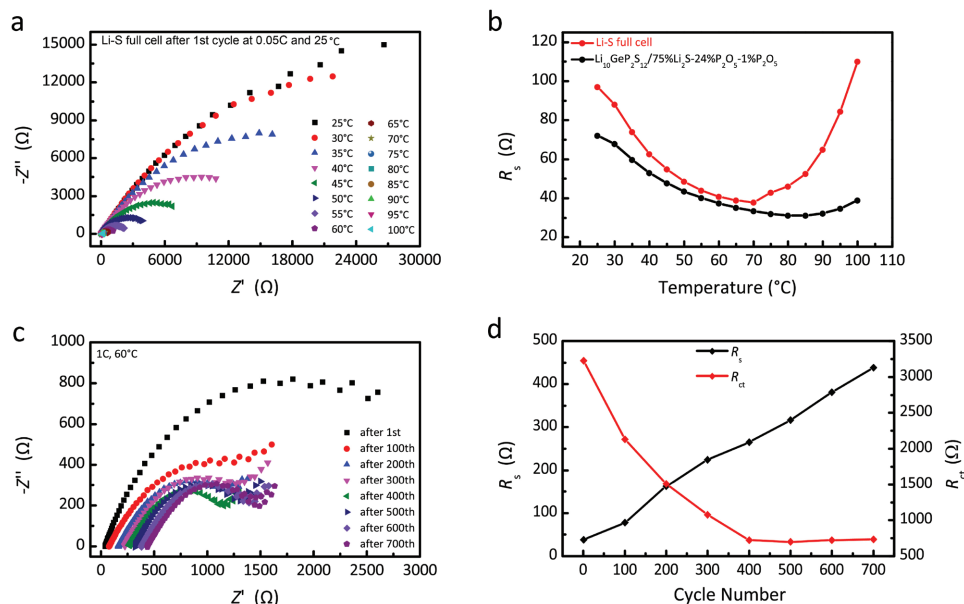


**Figure 7.** a) EIS of amorphous  $\text{rGO@S-40-Li}_{10}\text{GeP}_2\text{S}_{12}\text{-AB/Li}_{10}\text{GeP}_2\text{S}_{12}/75\%\text{Li}_2\text{S-24}\%\text{P}_2\text{S}_5\text{-1}\%\text{P}_2\text{O}_5/\text{Li}$  full cell. b) The ionic resistances of the Li-S full cell and bilayer electrolyte at different temperature. c) EIS of the Li-S full cell at different cycles at 1.0 C and 60 °C. d) The ionic and interface resistances of Li-S full cell at different cycles deduced from (c).

Information). The ionic resistance ( $R_s$ ) and the charge transfer resistance ( $R_{ct}$ ) are determined by fitting the EIS data with an equivalent circuit (Figure S7d, Supporting Information).<sup>[24,44]</sup> The intercept at the real Z-axis in the high frequency corresponds to the ionic resistance, while the semicircle in the middle frequency range corresponds to the charge transfer and solid electrolyte interphase (SEI) resistance at the interfaces. The latter is induced by the side reaction between electrode and electrolyte. For the bilayer electrolyte,  $R_s$  originates from the resistance of the solid electrolyte layer, while for Li-S full cell, the  $R_s$  are the total ionic resistance including both in electrolyte layer and in the electrode layer. The charge transfer resistance ( $R_{ct}$ ) in the Li-S full cell can be ascribed to the interfacial resistance in both cathode and anode layers. Due to the significantly improved stability between  $75\%\text{Li}_2\text{S-24}\%\text{P}_2\text{S}_5\text{-1}\%\text{P}_2\text{O}_5$  electrolyte and lithium metal,<sup>[25]</sup>  $R_{ct}$  here mainly originates from the reaction between  $\text{rGO@S-40}$  and  $\text{Li}_{10}\text{GeP}_2\text{S}_{12}$  solid electrolytes in cathode layer. The  $R_s$  values of bilayer electrolyte (Figure S7a, Supporting Information) and Li-S full cell (Figure S7b, Supporting Information) at different temperatures are compared in Figure 7b. For Li-S full cell, the obtained ionic resistances  $R_s$  initially decrease with increase of temperature and reach minimum value at 70 °C, and then begin to increase above 70 °C. Similar trend is observed in ionic resistance changes of  $\text{Li}_{10}\text{GeP}_2\text{S}_{12}/75\%\text{Li}_2\text{S-24}\%\text{P}_2\text{S}_5\text{-1}\%\text{P}_2\text{O}_5$  bilayer electrolyte, indicating the resistance in the electrolyte controls the cell performance. For a solid electrolyte, the ionic resistance normally decreases with increase of temperature. The high ionic resistance of Li-S cell at 25 °C is due to the poor ionic conductivity of solid-state electrolytes. To understand the reason for increase in ionic resistance of  $\text{Li}_{10}\text{GeP}_2\text{S}_{12}/75\%\text{Li}_2\text{S-24}\%\text{P}_2\text{S}_5\text{-1}\%\text{P}_2\text{O}_5$  bilayer above 70 °C, the structure of  $\text{Li}_{10}\text{GeP}_2\text{S}_{12}$  and  $75\%\text{Li}_2\text{S-24}\%\text{P}_2\text{S}_5\text{-1}\%\text{P}_2\text{O}_5$  at 25 and 100 °C for 12 h was characterized using XRD

(Figure S8, Supporting Information). The  $\text{Li}_{10}\text{GeP}_2\text{S}_{12}$  electrolyte shows high structure stability at 100 °C. However, some  $75\%\text{Li}_2\text{S-24}\%\text{P}_2\text{S}_5\text{-1}\%\text{P}_2\text{O}_5$  electrolyte decomposed to phosphorus and sulfur after being heat treated at 100 °C for 12 h, as demonstrated by characteristic peaks of both phosphorus and sulfur in Figure S8b (Supporting Information), which significantly increased the ionic resistance in Li-S cell. Currently, the exact mechanism for the electrolyte decomposition is not well understood. A detailed study for this issue is still undergoing. Clearly, the resistance increase of electrolyte bilayer above 70 °C is attributed to electrolyte decomposition. In addition, as shown in Figure 7b, the  $R_s$  of Li-S full cell at 60 and 100 °C are 40.9 and 110 Ω, respectively, while the  $R_s$  of electrolyte bilayer at 60 and 100 °C are 37.4 and 39 Ω, respectively. The  $R_s$  at 100 °C (110 Ω) for the Li-S full cell is much larger than that at 60 °C (40.9 Ω). When temperature increases from 60 to 100 °C, the  $R_s$  of Li-S full cell increases from 40.9 to 110 Ω, which is much higher than the resistance increase of electrolyte bilayer (from 37.4 to 39 Ω). Therefore, the side reactions between electrolyte and positive/negative electrode may occur. The XRD patterns for both cathode and lithium anode layers of the Li-S full cell cycled at 100 °C and 1.0 C for ten cycles are shown in Figure S9 (Supporting Information). Although it has been reported that doping  $\text{Li}_3\text{PS}_4$  with  $\text{P}_2\text{O}_5$  could greatly improve the compatibility between electrolyte and lithium metal,<sup>[25]</sup> some impurities could still be detected at lithium anode after cycling, which may be probable due to the instability of  $75\%\text{Li}_2\text{S-24}\%\text{P}_2\text{S}_5\text{-1}\%\text{P}_2\text{O}_5$  electrolyte at 100 °C as mentioned above. For the cathode layer, a significant XRD pattern change was observed after cycling, indicating the side reaction occurred at the cathode layer.<sup>[45]</sup> The increase in ionic resistance at 100 °C as well as the side reactions between electrolyte and positive/negative electrode cause the low and rapid capacity decay for amorphous  $\text{rGO@S-40}$  composite at 100 °C.



The Li-S cell with rGO@S-40 cathode shows the high capacity and long cycling stability. However, the full cell capacity still decays after 400 cycles. The mechanism for capacity change of Li-S full cell at 60 °C and 1.0 C rate (Figure 6d) was also investigated using EIS (Figure 7c). The ionic resistances and charge transfer resistance at different cycles are obtained from EIS in Figure 7c and shown in Figure 7d. During charge/discharge cycles, the ionic resistance continuously increases due to the stress/strain in the electrolyte induced by repeat volume change, while the interface resistance decreases before 400 cycles and then level off. The decrease in the interface resistance before 400 cycles is probably attributed to improved contact between rGO@S and electrolyte due to the volume expansion of rGO@S. The combination of ionic resistance and interface resistance controls the capacity of the full cell in the charge/discharge cycles. In the first 100 cycles, the ionic resistance slightly increases from 38.2 to 78  $\Omega$  arising from the volume and stress/strain changes, while the charge transfer resistance dramatically decreases from 3224 to 2129  $\Omega$  due to the activation process, leading to a capacity increase. From 100 to 400 cycles, the ionic resistance gradually increases but charge transfer resistance decreases, making a stable reversible capacity. However, after 400 cycles, the ionic resistance continues to increase, while the charge transfer resistance levels off, leading to a capacity decay. Upon continual cycling, the increased stress/strain can generate crack in both electrode and the electrolyte and eventually pulverize the electrode and electrolyte into powders, as demonstrated in Figure 8.

Clearly, the amorphous rGO@S-40 composite shows excellent electrochemical performances at 60 °C, which could benefit from the well-designed ultrathin sulfur that well contact both high electronic conductive rGO and high ionic conductive  $\text{Li}_{10}\text{GeP}_2\text{S}_{12}$  electrolyte ensuring fast electron and ion conduction, leading to high specific capacity and excellent power performances. In addition, the uniformly dispersed rGO@S-40 into  $\text{Li}_{10}\text{GeP}_2\text{S}_{12}$  electrolyte also generates even volume change

in the cathode, reducing the stress/strain and extending the cycling stability.

### 3. Conclusion

We coated a nanolayer of amorphous sulfur on electronic conductive rGO and then uniformly distributed these rGO@S composites into superionic conductive  $\text{Li}_{10}\text{GeP}_2\text{S}_{12}$  to achieve both high ionic and electronic conductivities, reduce the lithium ion diffusion length and stress/strain in the cathodes. The all-solid-state Li-S full cell employing an rGO@S- $\text{Li}_{10}\text{GeP}_2\text{S}_{12}$ -AB cathode,  $\text{Li}_{10}\text{GeP}_2\text{S}_{12}$ /75% $\text{Li}_2\text{S}$ -24% $\text{P}_2\text{S}_5$ -1% $\text{P}_2\text{O}_5$  bilayer as electrolyte, and lithium as the anode was evaluated at temperatures of 25, 60, and 100 °C. At 60 °C, the all-solid-state Li-S batteries using the amorphous rGO@S-40 composite show a very high initial discharge capacity of 1629  $\text{mA h g}^{-1}$  at a current density of 0.05 C, which is close to its theoretical capacity, corresponding to a sulfur utilization ratio of about 97.3%. With increasing current densities to 0.1, 0.5, 1.0, 2.0, and 5.0 C, it can still deliver discharge capacities of 1384.5, 1336.3, 903.2, 502.6, and 204.7  $\text{mA g}^{-1}$ . At 1.0 C, a high discharge capacity of 830  $\text{mA g}^{-1}$  was retained after 750 cycles, demonstrating excellent long-term cycling stability. The mechanisms for the capacity changes at different temperatures and different cycles were revealed using EIS, demonstrating that the reducing stress/strain through small and uniform volume change is critical for high-performance all-solid-state Li-S batteries.

### 4. Experimental Section

**Preparation of rGO@S Composites:** Sulfur deposited on reduced graphene oxide composites were synthesized according to a sulfur-amine chemistry method.<sup>[46]</sup> Typically, 25 mg of rGO (Nanjing JC Nano Tech Co., Ltd.) was dispersed in a mixture of deionized water and ethanol (10/1, v/v) through ultrasonication for 30 min. Then, sulfur-ethylenediamine complex solutions, containing a certain amount of sublimed sulfur and 5 mL anhydrous ethylenediamine,<sup>[46,47]</sup> were dropped into the rGO solution under stirring. After that, the above solutions were continuously stirred for 2 min. During this process, the sulfur-ethylenediamine complex decomposes to sulfur and deposits on the surface of rGO nanosheet. Finally, the obtained solution was filtrated, washed and dried under vacuum. Due to rapid reaction rate of sulfur recovery reaction from sulfur-ethylenediamine complex solution, the sulfur is easy to crystallize with increasing reaction time.<sup>[46–48]</sup> By carefully controlling the amount of sublimed sulfur and reaction time, different kinds of composites can be obtained. Here, rGO loaded with around 50 wt% amorphous sulfur, 40 wt% amorphous sulfur, and 40 wt% crystal sulfur were denoted as amorphous rGO@S-50, amorphous rGO@S-40, and crystal rGO@S-40.

The synthesis of  $\text{Li}_{10}\text{GeP}_2\text{S}_{12}$  and 75% $\text{Li}_2\text{S}$ -24% $\text{P}_2\text{S}_5$ -1% $\text{P}_2\text{O}_5$  solid electrolytes can be found elsewhere.<sup>[25,49]</sup>

**Materials Characterization:** XRD measurements were carried out using a Bruker AXS D8 Advance with Cu K $\alpha$  radiation ( $\lambda = 1.54178 \text{ \AA}$ ). Raman spectra were measured with a Renishaw in Via-Reflex Raman spectrophotometer. The morphology and structure were analyzed by a Hitachi S-4800 field emission SEM equipped with EDX and an FEI Tecnai G<sup>2</sup> F20 TEM at an accelerating voltage of 200 kV. AFM images were recorded using a Veeco Dimension3100V scanning probe microscope at ambient conditions using the tapping mode. TGA were performed using a thermal analyzer (Diamond TG, PerkinElmer, USA) under nitrogen protection with a heating rate of 5 °C min<sup>-1</sup>. Sulfur content was also determined by a carbon sulfur analyzer (CS844, LECO, USA).

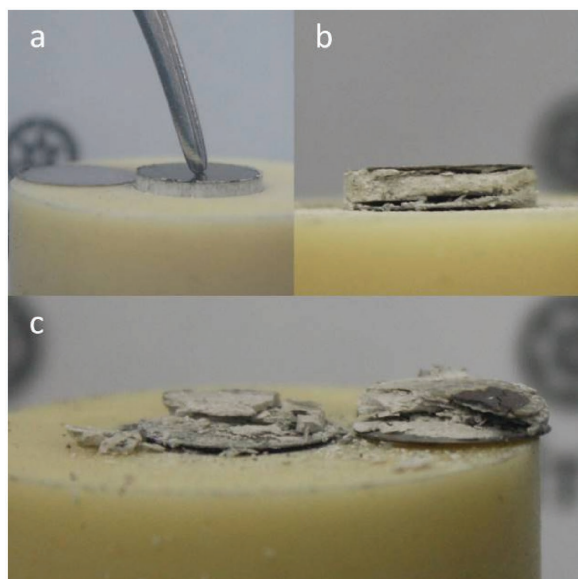


**Figure 8.** Photograph of the Li-S full cells a) before and b,c) after 750 cycles at 1.0 C and 60 °C.

**Electrochemical Performance Measurements:** Laboratory-scale all-solid-state cells were constructed by employing rGO@S composites in combination with  $\text{Li}_{10}\text{GeP}_2\text{S}_{12}$  and AB as the cathode, together with a lithium anode and a solid electrolyte bilayer located between the cathode and the anode.<sup>[20,29,50]</sup> For composite cathode electrodes, the as-synthesized rGO@S powders were mixed with the  $\text{Li}_{10}\text{GeP}_2\text{S}_{12}$  and AB with the weight ratio of 30:50:20 by ball-milling for 20 h. The all-solid-state cells were fabricated as follows: 100 mg of the  $\text{Li}_{10}\text{GeP}_2\text{S}_{12}$  and 50 mg of 75% $\text{Li}_2\text{S}$ -24% $\text{P}_2\text{S}_5$ -1% $\text{P}_2\text{O}_5$  were pressed successively under 240 MPa to form solid electrolyte bilayer with the thicknesses of around 670 and 330  $\mu\text{m}$ , respectively. Then, the cathode composite powder was uniformly spread onto the side of  $\text{Li}_{10}\text{GeP}_2\text{S}_{12}$  layer and pressed under 240 MPa. The mass loading of cathode is about 3.5  $\text{mg cm}^{-2}$ , corresponding to a sulfur loading of 0.4–0.5  $\text{mg cm}^{-2}$  in cathode. Finally, the Li foil was attached to the side of 75% $\text{Li}_2\text{S}$ -24% $\text{P}_2\text{S}_5$ -1% $\text{P}_2\text{O}_5$  by pressing under 360 MPa. All the processes were performed in an argon-filled glove box.

Electrochemical performances of the rGO@S composites in the all-solid-state lithium batteries were investigated by galvanostatic charge–discharge tests at different C rate ( $1\text{ C} = 1675\text{ mA g}^{-1}$ ) by using a multichannel battery test system (LAND CT-2001A, Wuhan Rambo Testing Equipment Co., Ltd.) under a cut-off voltage of 1.5–2.8 V. The temperature was controlled in a constant temperature oven. The specific capacities were calculated based on the mass of sulfur. CV and EIS were recorded on a Solartron 1470E (Solartron Public Co., Ltd.) multichannel potentiostat electrochemical workstation.

## Supporting Information

Supporting Information is available from the Wiley Online Library or from the author.

## Acknowledgements

X.Y. and N.H. contributed equally to this work. This work was supported by funding from the Strategic Priority Research Program of the Chinese Academy of Sciences (Grant No. XDA09010201), the National Natural Science Foundation of China (Grant No. 51502317), and Youth Innovation Promotion Association CAS (2017342). Dr. C. Wang would like to acknowledge the financial support from Army Research Office (Program Manager: Dr. Robert Mantz) under Award No. W911NF1510187.

## Keywords

lithium–sulfur batteries, cycling stability, reduced graphene oxide, sulfide electrolyte, amorphous sulfur

Received: December 28, 2016  
Revised: February 16, 2017  
Published online: May 11, 2017

- [1] X. L. Ji, K. T. Lee, L. F. Nazar, *Nat. Mater.* **2009**, 8, 500.
- [2] V. Etacheri, R. Marom, R. Elazari, G. Salitra, D. Aurbach, *Energy Environ. Sci.* **2011**, 4, 3243.
- [3] A. Manthiram, Y. Z. Fu, S. H. Chung, C. X. Zu, Y. S. Su, *Chem. Rev.* **2014**, 114, 11751.
- [4] D. Bresser, S. Passerini, B. Scrosati, *Chem. Commun.* **2013**, 49, 10545.
- [5] Y. Yang, G. Y. Zheng, Y. Cui, *Chem. Soc. Rev.* **2013**, 42, 3018.

- [6] Y. X. Yin, S. Xin, Y. G. Guo, L. J. Wan, *Angew. Chem., Int. Ed.* **2013**, 52, 13186.
- [7] B. Zhang, X. Qin, G. R. Li, X. P. Gao, *Energy Environ. Sci.* **2010**, 3, 1531.
- [8] J. C. Guo, Y. H. Xu, C. S. Wang, *Nano Lett.* **2011**, 11, 4288.
- [9] L. F. Xiao, Y. L. Cao, J. Xiao, B. Schwenzer, M. H. Engelhard, L. V. Saraf, Z. M. Nie, G. J. Exarhos, J. Liu, *Adv. Mater.* **2012**, 24, 1176.
- [10] Y. M. Lee, N. S. Choi, J. H. Park, J. K. Park, *J. Power Sources* **2003**, 119, 964.
- [11] Z. Lin, Z. C. Liu, W. J. Fu, N. J. Dudney, C. D. Liang, *Adv. Funct. Mater.* **2013**, 23, 1064.
- [12] Z. Lin, C. D. Liang, *J. Mater. Chem. A* **2015**, 3, 936.
- [13] Z. Lin, Z. C. Liu, N. J. Dudney, C. D. Liang, *ACS Nano* **2013**, 7, 2829.
- [14] Z. Lin, Z. C. Liu, W. J. Fu, N. J. Dudney, C. D. Liang, *Angew. Chem., Int. Ed.* **2013**, 52, 7460.
- [15] F. Han, J. Yue, X. Fan, T. Gao, C. Luo, Z. Ma, L. Suo, C. Wang, *Nano Lett.* **2016**, 16, 4521.
- [16] M. Nagao, A. Hayashi, M. Tatsumisago, *Electrochim. Acta* **2011**, 56, 6055.
- [17] S. Kinoshita, K. Okuda, N. Machida, T. Shigematsu, *J. Power Sources* **2014**, 269, 727.
- [18] H. Nagata, Y. Chikusa, *J. Power Sources* **2014**, 264, 206.
- [19] A. Unemoto, C. L. Chen, Z. C. Wang, M. Matsuo, T. Ikeshoji, S. Orimo, *Nanotechnology* **2015**, 26, 254001.
- [20] X. Yao, D. Liu, C. Wang, P. Long, G. Peng, Y. Hu, H. Li, L. Chen, X. Xu, *Nano Lett.* **2016**, 16, 7148.
- [21] X. Y. Yao, B. X. Huang, J. Y. Yin, G. Peng, Z. Huang, C. Gao, D. Liu, X. X. Xu, *Chin. Phys. B* **2016**, 25, 018802.
- [22] M. Tatsumisago, M. Nagao, A. Hayashi, *J. Asian Ceram. Soc.* **2013**, 1, 17.
- [23] T. Kobayashi, Y. Imade, D. Shishihara, K. Homma, M. Nagao, R. Watanabe, T. Yokoi, A. Yamada, R. Kanno, T. Tatsumi, *J. Power Sources* **2008**, 182, 621.
- [24] T. Yamada, S. Ito, R. Omoda, T. Watanabe, Y. Aihara, M. Agostini, U. Ulissi, J. Hassoun, B. Scrosati, *J. Electrochem. Soc.* **2015**, 162, A646.
- [25] Y. C. Tao, S. J. Chen, D. Liu, G. Peng, X. Y. Yao, X. X. Xu, *J. Electrochem. Soc.* **2016**, 163, A96.
- [26] X. Y. Tao, F. Chen, Y. Xia, H. Huang, Y. P. Gan, X. R. Chen, W. K. Zhang, *Chem. Commun.* **2013**, 49, 4513.
- [27] P. D. Harvey, I. S. Butler, *J. Raman Spectrosc.* **1986**, 17, 329.
- [28] A. Sadezky, H. Muckenhuber, H. Grothe, R. Niessner, U. Poschl, *Carbon* **2005**, 43, 1731.
- [29] H. Wan, G. Peng, X. Yao, J. Yang, P. Cui, X. Xu, *Energy Storage Mater.* **2016**, 4, 59.
- [30] Y. H. Xu, Y. Wen, Y. J. Zhu, K. Gaskell, K. A. Cychoz, B. Eichhorn, K. Xu, C. S. Wang, *Adv. Funct. Mater.* **2015**, 25, 4312.
- [31] X. Yang, L. Zhang, F. Zhang, Y. Huang, Y. S. Chen, *ACS Nano* **2014**, 8, 5208.
- [32] W. Weng, V. G. Pol, K. Amine, *Adv. Mater.* **2013**, 25, 1608.
- [33] L. N. Wang, Y. Zhao, M. L. Thomas, H. R. Byon, *Adv. Funct. Mater.* **2014**, 24, 2248.
- [34] T. Takeuchi, H. Kageyama, K. Nakanishi, M. Tabuchi, H. Sakaebe, T. Ohta, H. Senoh, T. Sakai, K. Tatsumi, *J. Electrochem. Soc.* **2010**, 157, A1196.
- [35] R. A. Sharma, *J. Electrochem. Soc.* **1972**, 119, 1439.
- [36] F. D. Han, T. Gao, Y. J. Zhu, K. J. Gaskell, C. S. Wang, *Adv. Mater.* **2015**, 27, 3473.
- [37] Q. Wang, N. Yan, M. Wang, C. Qu, X. Yang, H. Zhang, X. Li, H. Zhang, *ACS Appl. Mater. Interfaces* **2015**, 7, 25002.
- [38] S. Zhang, N. Li, H. Lu, J. Zheng, R. Zang, J. Cao, *RSC Adv.* **2015**, 5, 50983.
- [39] C. Zhang, Y. Lin, J. Liu, *J. Mater. Chem. A* **2015**, 3, 10760.
- [40] G. He, X. L. Ji, L. Nazar, *Energy Environ. Sci.* **2011**, 4, 2878.



- [41] J. Schuster, G. He, B. Mandlmeier, T. Yim, K. T. Lee, T. Bein, L. F. Nazar, *Angew. Chem., Int. Ed.* **2012**, 51, 3591.
- [42] H. Chen, C. Wang, Y. Dai, S. Qiu, J. Yang, W. Lu, L. Chen, *Nano Lett.* **2015**, 15, 5443.
- [43] J. Liu, W. Li, L. Duan, X. Li, L. Ji, Z. Geng, K. Huang, L. Lu, L. Zhou, Z. Liu, W. Chen, L. Liu, S. Feng, Y. Zhang, *Nano Lett.* **2015**, 15, 5137.
- [44] Z. Deng, Z. Zhang, Y. Lai, J. Liu, J. Li, Y. Liu, *J. Electrochem. Soc.* **2013**, 160, A553.
- [45] F. Han, Y. Zhu, X. He, Y. Mo, C. Wang, *Adv. Energy Mater.* **2016**, 6, 1501590.
- [46] H. W. Chen, C. H. Wang, W. L. Dong, W. Lu, Z. L. Du, L. W. Chen, *Nano Lett.* **2015**, 15, 798.
- [47] R. E. Davis, H. F. Nakshbendi, *J. Am. Chem. Soc.* **1962**, 84, 2085.
- [48] C. Wang, H. Chen, W. Dong, J. Ge, W. Lu, X. Wu, L. Guo, L. Chen, *Chem. Commun.* **2014**, 50, 1202.
- [49] J. Y. Yin, X. Y. Yao, G. Peng, J. Yang, Z. Huang, D. Liu, Y. C. Tao, X. X. Xu, *Solid State Ionics* **2015**, 274, 8.
- [50] P. Long, Q. Xu, G. Peng, X. Y. Yao, X. X. Xu, *ChemElectroChem* **2016**, 3, 764.